

Chem-SIM: Super-resolution Chemical Imaging via Photothermal Modulation of Structured-Illumination Fluorescence

Dashan Dong^{1,2}, Danchen Jia^{1,2}, Xinyan Teng³, Jianpeng Ao^{1,2}, George Abu-Aqil¹,
Biwen Gao³, Meng Zhang^{1,2}, Qing Xia^{1,2}, Ji-Xin Cheng^{1,2,3,4,*}

¹ Department of Electrical and Computer Engineering, Boston University, Boston, Massachusetts 02215, United States;

² Photonics Center, Boston University, Boston, Massachusetts 02215, United States;

³ Department of Chemistry, Boston University, Boston, Massachusetts 02215, United States;

⁴ Department of Biomedical Engineering, Boston University, Boston, Massachusetts 02215, United States.

* Correspondence: jxcheng@bu.edu (J.-X.C.)

Abstract

Structured illumination microscopy (SIM) has attained high spatiotemporal delineation of subcellular architecture, yet offers limited insight into chemical composition. Here, we present Chem-SIM, a structured-illumination fluorescence detected mid-infrared photothermal microscopy, for super-resolution chemical imaging of microorganisms and mammalian cells. A computational pipeline combining Poisson maximum-likelihood demodulation and spectral normalization across wavenumber is implemented to robustly recover the weak IR-induced fluorescence intensity change under low photon budgets and convert the fluorescence intensity modulation to chemical fingerprints. A photothermal gating scheme further rejects water backgrounds in aqueous samples, while the IR pump maintains cellular activity at near-physiological temperature. Chem-SIM preserves full vibrational fingerprints, achieves SIM-grade lateral resolution, and operates in a high-throughput, camera-based format with minimal modifications and low photothermal load. At the single-bacterium level, Chem-SIM distinguishes stationary phase from log phase cells through chemical content mapping. In ovarian cancer cells, Chem-SIM delivers readouts of lipid chemistry under deuterium fatty acid treatment and resolves lipid droplets dynamics in live cells. Together, Chem-SIM provides an accessible route to super-resolved mapping of organelle chemistry, metabolism, and dynamics.

Main

Organelles partition intracellular processes in space and function, coordinating discrete metabolic pathways and mediating the exchange of materials and information^{1, 2}. Recent advances in super-resolution fluorescence microscopy have permitted visualization of individual organelles in living cells at sub-100 nm lateral resolution³. Among these modalities, structured-illumination microscopy (SIM) is well suited to live-cell studies because it provides two-fold resolution enhancement with camera-based acquisition with low phototoxicity⁴⁻⁶. By employing multicolor fluorescent tags with SIM, researchers have inferred organelle interactions from their physical contacts^{1, 7, 8} and enrich extra dimensions through modalities such as fluorescence lifetime⁹, single-molecule photophysics¹⁰, and dipole-orientation analysis^{11, 12}.

Fluorescence microscopy, however, only visualizes selected chromophores and therefore cannot reveal molecular composition of organelles for function analysis. Advanced vibrational microscopies¹³, including coherent Raman scattering¹⁴ and mid-infrared photothermal (MIP) microscopy¹⁵, together with vibration probes¹⁶, provide molecular contrast by probing chemical bond vibrations. Super-resolution coherent Raman imaging via single-pixel detection and structured illumination has been demonstrated on biological specimens¹⁷⁻¹⁹, whereas the coherent Raman methods require complex ultrafast lasers and remain throughput-limited by point scanning. By contrast, MIP exploits infrared (IR) absorption with cross-sections orders of magnitude larger than those of Raman scattering, uses pump–probe detection to reach sub-micron resolution, and can be implemented in wide-field configurations for high-throughput chemical imaging²⁰⁻²³.

In wide-field MIP, a camera detects photothermal modulation of scattering while an IR laser illuminates the full field of view, maximizing IR-energy use²⁴; synthetic-aperture computation

extends the resolution into three dimensions^{25, 26}. Nonetheless, shallow modulation of scattered photons limits its sensitivity²⁷. Fluorescence-detected MIP (F-MIP) mitigates this issue by using fluorescent dyes as nanoscale thermometers, increasing modulation depth by two orders of magnitude²⁸⁻³². By integrating F-MIP with structured illumination, the technique can surpass the visible diffraction limit³³. Yet, strong water absorption³⁴ and limited fluorescence photon budgets^{28, 31} in living specimens have thus far hindered super-resolution wide-field photothermal imaging in aqueous environments, despite proof-of-concept demonstrations on dried polymer beads³³.

Here, we present Chem-SIM, a wide-field MIP-modulated structured-illumination fluorescence platform for super-resolution chemical imaging in both fixed and live cells. By integrating sinusoidal illumination with Poisson maximum-likelihood demodulation, Chem-SIM achieves $\sim 2\times$ lateral resolution while boosting sensitivity over previously reported wide-field F-MIP. Our approach preserves full vibrational fingerprints under photon-limited conditions and suppresses water background through photothermal relaxation gating. Notably, the IR pump maintains a near-physiological temperature during acquisition to help sustain cellular activity. With such capacities, Chem-SIM enables fingerprint-level readout of metabolism and chemistry in single bacterial and single organelles. Chem-SIM requires only minimal modifications to a standard wide-field microscope, and provides a platform for high-throughput mapping of organelle chemistry, metabolism, and dynamics.

Results

Principle and implementation of Chem-SIM

Chem-SIM integrates mid-infrared (mid-IR) photothermal excitation with structured-illumination microscopy to deliver super-resolution, wide-field chemical imaging. As shown in **Figure 1a**, the system adopts an upright wide-field layout optimized for calcium fluoride (CaF_2) substrates. A tunable 50 kHz mid-IR quantum cascade laser (QCL) excites molecular vibrations. A nanosecond-pulsed visible laser is patterned by a digital micromirror device (DMD) to encode high-spatial-frequency content beyond the diffraction limit. Photothermal-induced fluorescence modulation is acquired in alternating “hot” (IR on) and “cold” (IR off) frames that are pulse-synchronized via electronic gating (**Figure 1b**). Hundreds of pump–probe cycles are averaged per frame to approach shot-noise-limited fluorescence detection by an sCMOS camera. Full details of the optical and electronic components are provided in the *Methods*.

For each Chem-SIM acquisition, three pattern orientations and three phase shifts yield nine hot and nine cold images. These raw frames are reconstructed using a joint RL–SIM algorithm, which preserves quantitative modulation contrast (detailed in **Supplementary Note 1** and **Supplementary Figure 1**), and the resulting hot-SIM and cold-SIM images are then subtracted pixel-wise to extract the thermally modulated signal (**Figure 1c**). For hyperspectral imaging, the mid-IR pump is stepped from $900-1798\text{ cm}^{-1}$ in 1 cm^{-1} increments; at each wavenumber we record the full 18-frame sequence at speed of 40 fps with an effective exposure of 23.1 ms per frame, giving a total acquisition time of ~ 585 s for the entire stack (detailed in **Supplementary Note 2**). As shown in **Figure 1d**, cold-SIM exhibits $\sim 20\%$ photobleaching over the scan, whereas hot-SIM additionally encodes wavelength-dependent IR absorption. The modulation-depth spectrum is obtained from the cold–hot subtraction after normalizing by the cold-SIM bleaching curve and it

reveals water-vapor absorption lines along the optical path, consistent with the on-sample IR power spectrum (**Figure 1e**). Finally, a weighted least-squares normalization of this modulation-depth spectrum by the measured on-sample IR power both equalizes wavenumber-dependent pump power and effectively suppresses water-vapor absorption lines, producing the Chem-SIM absorption spectrum (**Figure 1f**) that closely matches the normalized reference Fourier transform infrared (FTIR) spectrum. Full details of spectrum normalization are provided in the *Methods*, **Supplementary Note 3**, and **Supplementary Figure 2**.

High-Quality Chem-SIM by Poisson Maximum-Likelihood Demodulation

Despite the high-quality area-averaged Chem-SIM spectra (**Figure 1f**), single-pixel Cold–Hot images remain dominated by noise and contain little usable modulation contrast. Mid-IR absorption induces only a small temperature rise that weakly perturbs the local fluorescence yield (< 10% on average). As shown in **Figure 2a**, the raw hot and cold frames have sufficient signal-to-noise ratio (SNR) to reveal the structured-illumination fringes; however, their cold–hot subtraction is noise-amplifying and fails to recover these patterns. The same holds when hot and cold stacks are reconstructed separately by SIM and then subtracted. The resulting difference image remains noisy and the high-resolution modulation contrast is severely degraded. This behavior is expected, because differencing two Poisson-distributed measurements produces a Skellam-distributed signal whose variance scales with the sum of the counts, degrading SNR when the modulation depth is shallow. Averaging multiple hot/cold pairs is a conventional way to suppress such noise; however, boosting the modulation SNR by an order of magnitude would require averaging over many pixels spectrally or ~100-fold higher fluorescence photon flux. Such spectral averaging or using an increased photon budget is not practical because it compromises the spectral resolution or exacerbates photobleaching.

Modern sCMOS cameras deliver shot-noise-limited performance when operated with high-sensitivity ADCs that saturate at ~1100 counts, providing sufficient dynamic range for most fluorescence imaging at modest photon budgets³⁵. Resolving small photothermal modulation signals, however, is substantially more demanding. As shown in **Figure 2b**, hot and cold pixel counts are well modeled as Poisson variates, and their difference follows a Skellam distribution³⁶. Even near saturation of the cold channel (~1000 counts), the effective dynamic range compresses cold–hot differences into a narrow band (~20 to 200 counts), so naïve frame differencing amplifies noise, depresses contrast/SNR, and can yield spurious negative-valued artifacts. Importantly, **Figure 2b** also compares multiple modulation-depth scenarios whose differential signals overlap within this band, indicating a strong coupling between modulation depth (chemistry) and cold fluorescence (brightness). The bright regions with weak modulation can mimic dim regions with strong modulation, confounding chemical contrast by simple differencing.

To address these limitations, we developed a likelihood-based demodulation strategy that exploits the full hot/cold photon statistics together with the SIM forward model. Specifically, we introduce a Poisson maximum-likelihood demodulation (P-MLD) framework³⁷ that jointly models the unmodulated fluorescence and the IR-induced modulation under structured illumination (**Figure 2c**). Let $x \geq 0$ denote the baseline (cold) fluorescence map, and let $0 \leq m \leq 1$ denote a

dimensionless modulation map such that the Hot fluorescence map is given by the element-wise product $m \odot x$. The photothermal modulation image used as the chemical-contrast channel is defined as the cold–hot difference $z \equiv x - m \odot x$. For each structured-illumination pattern, we adopt a standard SIM forward model that multiplies x by the pattern, convolves with the system point-spread function, and adds a slowly varying background term. Each pixel in all hot and cold frames is treated as a Poisson random variable whose mean is given by this forward model, and P-MLD seeks nonnegative x , m , and background that maximize the joint Poisson likelihood of all frames; we solve the resulting inverse problem using a nonnegative Richardson–Lucy–style multiplicative algorithm (detailed in *Methods* and **Supplementary Note 4**).

Figure 2d–g benchmarks P-MLD against conventional differencing on the same dataset. Applied to a single raw structured-illumination hot/cold pair, P-MLD suppresses spurious negatives, enhances local SNR, and cleanly recovers the fringe pattern (**Figure 2d**). Using the full 3-orientation \times 3-phase dataset, SIM-based P-MLD produces a higher-resolution modulation image that resolves finer features, with an SNR improvement of \sim 20 dB compared with pixel-wise cold–hot subtraction (**Figure 2e** and detailed in **Supplementary Note 5**). At the single-pixel level, P-MLD markedly reduces spectral noise (**Figure 2f**). After applying spectral normalization described in the previous section, the recovered high-SNR vibrational spectrum closely matches the area-averaged Chem-SIM spectrum (**Figure 2g**). Together, these results demonstrate that P-MLD enables high-fidelity Chem-SIM mapping at each wavenumber without increasing the photon budget or compromising spectral resolution.

Spatial and spectroscopic mapping of single *Staphylococcus aureus*

We first applied Chem-SIM to *Staphylococcus aureus* (*S. aureus*) labeled with rhodamine 6G and mounted on CaF_2 coverslips (**Figure 3**). For a fair comparison under identical photon budgets, nine patterned raw frames were averaged to synthesize the equivalent cold/hot wide-field fluorescence (WF-FL) images, and an F-MIP image was obtained by cold–hot subtraction. The Chem-SIM images are computed from the same raw data using the P-MLD algorithm with structured illumination. In **Figure 3a–d**, as expected for SIM, WF-FL provides only a blurred outline of individual cocci, whereas SIM resolves the granular cell-wall morphology across the same field. Line profiles and Fourier ring correlation (FRC) analysis³⁸ (detailed in **Supplementary Note 6**) confirm an almost twofold gain in lateral resolution for SIM relative to WF-FL.

Probing the amide-I band (1650 cm^{-1}) produces chemical contrast in both F-MIP and Chem-SIM that is dominated by the mid-IR focus profile (**Figure 3e**). In the F-MIP images, however, the cold–hot subtraction leaves substantial high-frequency noise, individual cocci remain only weakly separated, and the apparent fine texture is largely noise-driven. By contrast, with P-MLD reconstruction, Chem-SIM recovers individual cells and subcellular texture with markedly enhanced SNR (**Figure 3f**). Due to additional noise from subtraction, the F-MIP images exhibit high-frequency fluctuations that do not follow the underlying fluorescence distribution (**Figure 3g**), and FRC analysis shows that this noise actually degrades the effective resolution from \sim 421 nm for WF-FL to \sim 708 nm for F-MIP (**Figure 3h**).

At the nucleic-acid band with lower modulation (1080 cm^{-1}), both F-MIP and Chem-SIM show markedly reduced signal levels (**Figure 3i**). Zoomed views (**Figure 3j**) and line profiles (**Figure 3k**) show that Chem-SIM retains lower noise and a spatial distribution that more closely tracks the fluorescence structure than F-MIP. As anticipated from the FRC benchmark of 214 nm (**Figure 3l**), Chem-SIM at both 1650 and 1080 cm^{-1} achieves SIM-like structural detail while preserving mid-IR spectral specificity. On the contrary, although F-MIP shows good contrast at strongly absorbing bands, it rapidly loses spatial discriminability at lower-modulation bands when based solely on cold-hot subtraction.

S. aureus is responsible for over 50% of human skin infections. Distinguishing between log and stationary phases of *S. aureus* is significant due to shifts in the bacterial virulence factor expression, metabolism, and antibiotic susceptibility. With much enhanced contrast and resolution in Chem-SIM, we next compared stationary-phase and log-phase populations at the single-coccus level. Chem-SIM maps at 1650 cm^{-1} (**Figure 3m**) reveal heterogeneous cellular chemistry, and single-bacterium-averaged Chem-SIM spectra (mean \pm s.e.m.) capture clear population-level trends (**Figure 3n**). During rapid growth, nucleic-acid synthesis elevates the PO_2^- band over amide-I band, as reflected in an increased $1080/1650\text{ cm}^{-1}$ intensity ratio for log-phase bacteria (**Figure 3o**). Together, these results show the potential of Chem-SIM not only for the detection of *S. aureus*, but also characterization of its metabolic activity.

Background Suppressed Chem-SIM Imaging in Aqueous Environment

Applying our Hot/Cold SIM-based Chem-SIM to HeLa cells in buffer, a strong signal for the ester C=O vibration at 1744 cm^{-1} was expected (**Figure 4a**). Instead, hyperspectral Chem-SIM shows that Cold-SIM traces follow normal photobleaching, whereas Hot-SIM modulation closely tracks the IR laser power spectrum, and even power-normalized spectra increase near the water absorption band at 1650 cm^{-1} (**Figure 4b**). Consistent with this, we observe distinct photothermal relaxation kinetics at the lipid carbonyl (C=O) band and at water-dominated bands (**Supplementary Figure 3**). Finite-element simulations support these observations. Under wide-field illumination, repeated mid-IR pulse trains establish a quasi-steady “heat zone” in the aqueous medium just above the CaF_2 substrate, slightly beyond the nominal penetration depth, which equilibrates on the millisecond timescale³⁴. Individual pump pulses still induce fast transient excursions on top of this background. Because bulk water is thermally coupled to this extended heat zone, it cools more slowly than small, thermally confined inclusions such as lipid droplets or 100-nm PMMA beads, leading to a delayed thermal transient at water-dominated bands (**Supplementary Note 7, Supplementary Figure 4 & Supplementary Movie 1**). Such thermal dynamics difference raises the opportunity of extracting small signals from the water absorption background in widefield photothermal imaging of aquatic samples.

Leveraging the slowly varying feature of water background, we introduce photothermal relaxation (PR) gating for wide-field photothermal imaging. Conceptually (**Figure 4c**), the pump pulse creates a fast temperature rise in the absorber (lipid) and a slower, spatially diffuse response in water. PR gating acquires two frames at two different probe delays, Delay 1 near the absorber peak and Delay 2 on the water-dominated tail, and forms a difference that cancels water background

while retaining target-specific contrast (**Supplementary Note 8 & Supplementary Figure 5-6**). PR gating is implemented electronically by shifting the mid-IR trigger relative to the probe, without additional boxcar hardware and without sacrificing wide-field throughput, and the two-delay frames are integrated into the P-MLD framework to yield PR gated Chem-SIM reconstructions that remain non-negative and resolution-enhanced.

Applied to Lipi-Red-stained HeLa cells, SIM provides the expected gain over WF-FL, yielding higher contrast and an approximately twofold improvement in lateral resolution (**Figure 4d-f**). With PR gating, the aqueous background is strongly suppressed in both F-MIP and Chem-SIM, isolating lipid droplets with high local contrast (**Figure 4g, h**). FRC analysis confirms that SIM-based wide-field imaging improves the fluorescence resolution by $\sim 2\times$, and that PR gated Chem-SIM provides an additional $\sim 4\times$ lateral resolution gain over PR gated F-MIP, enabled by the SNR increase from P-MLD (**Figure 4f, i**). PR gated Chem-SIM spectra (**Figure 4j**) from the eight individual droplet marked in **Figure 4h** consistently show a dominant ester C=O peak at 1744 cm^{-1} , together with other lipid bands³⁹ showing robust fingerprint-level specificity. The peak around 1650 cm^{-1} is assigned to residual water background. Together, these results demonstrate background-suppressed, super-resolved chemical imaging of lipid droplets in aqueous media without sacrificing photon budget or spectral fidelity.

Chem-SIM Unveils Lipid Chemistry in Cancer Cells

Ovarian cancer cells are known to accumulate lipids and gain aggressiveness in a lipid-rich environment^{40,41}. To explore the potential of Chem-SIM for imaging lipid chemistry inside ovarian cancer cells, OVCAR5 cells were first incubated in lipid-deficient medium and then treated with fully-deuterated palmitic acid-d₃₁ (PA-d₃₁) for different time periods. Chem-SIM spectra cover both the fingerprint region and the C–D “silent window” (**Figure 4k & Supplementary Figure 7**). After cell fixation with formaldehyde, hyperspectral Chem-SIM imaging was carried out. In the fingerprint region, lipid droplets display various signatures, including a prominent ester C=O band at 1744 cm^{-1} , CH₂ vibrations near 1464 cm^{-1} , and CH₃ vibrations near 1377 cm^{-1} . The band at $\sim 1164\text{ cm}^{-1}$ is assigned to C–O–C symmetric stretching in the glycerol backbone. In cells treated with lipid-deficient medium, an additional band appears near 1100 cm^{-1} , attributable to C–O stretching in C–OH groups of diacylglycerol (DAG) or monoacylglycerol (MAG) species produced by lipase-mediated triacylglycerol (TAG) hydrolysis under fatty-acid deprivation. The corresponding TAG, DAG structures and synthesis are shown in **Supplementary Figure 8**.

With increasing PA-d₃₁ incubation time, strong symmetric and antisymmetric C–D vibration bands emerge and grow in the silent window, indicating progressive incorporation of exogenous deuterated fatty acids into lipid droplets as a protective mechanism against lipotoxic stress⁴². In particular, compared with the PA-free cells, the antisymmetric C–O–C band near 1255 cm^{-1} is markedly enhanced, consistent with an increased population of asymmetric TAG species arising from deuterated acyl chains. By contrast, the C–O peak near 1100 cm^{-1} is much reduced. These systematic spectral changes in both silent and fingerprint windows report on strong TAG biosynthesis activity upon external palmitic acid treatment.

Chem-SIM allows dynamic imaging of live cells

A practical challenge for Chem-SIM imaging of live cells is cumulative heating from repeated mid-IR excitation, which can perturb cell physiology. In our implementation, live-cell Chem-SIM is enabled by actively constraining the thermal load in three ways. First, the use of a water-dipping objective and a relatively large imaging dish, together with water's high heat capacity, facilitates rapid thermal exchange between the field of view and the surrounding medium. Second, under fixed IR-pump conditions, our nanosecond probe timing is positioned close to the peak of the photothermal transient, maximizing modulation depth for a given average power. Third, each Chem-SIM frame integrates over ~4,500 pump pulses, providing high sensitivity to small temperature changes while averaging out laser and thermal noise. Fluorescence thermometry with Lipi-Red (**Supplementary Note 9** and **Supplementary Figures 9–10**) shows that the mean medium temperature during imaging scales with the mid-IR average power. At the lipid C=O absorption peak, the surrounding medium equilibrates at ~34 °C, while individual mid-IR pulse trains drive rapid excursions to ~38 °C that relax back to baseline within the interpulse interval.

With optimized heat control, we applied PR-gated Chem-SIM to track lipid droplets in live OVCAR5 cells over tens of minutes (**Figure 5a & Supplementary Movie 2**). SIM Lipi-Red images define the droplet morphology, whereas Chem-SIM maps at 1744 cm⁻¹ (ester C=O) and 2196 cm⁻¹ (C–D) report the endogenous lipid and deuterated TAG pools, respectively. Under IR-ON conditions, both C=O and C–D contrast are observed. The IR-OFF controls show a negligible Chem-SIM signal.

To examine the impact of IR exaction on cell physiology, we performed single-droplet tracking (**Figure 5b**), which yields time series that are well described by an anomalous-diffusion model^{43, 44}. From this data, we extracted the mean-squared displacement (MSD), anomalous exponent α , and generalized diffusion coefficient D . Box-plot summaries (**Figure 5c–d**) show that SIM-based wide-field imaging (IR-OFF), performed at room temperature of 20°C, preserves the expected super-diffusive motion of lipid droplets. Interestingly, IR illumination produces little change over the thermal-driven diffusion factor D (**Figure 5e**), indicating that Chem-SIM can monitor lipid-droplet dynamics with their native motility. Together, these results demonstrate that Chem-SIM allows background-suppressed, super-resolved, and dynamically compatible chemical imaging of living cells.

Discussion

By mid-IR photothermal modulation of structured-illumination fluorescence and Poisson likelihood demodulation, Chem-SIM is developed to deliver chemical maps of single bacteria and single organelles beyond the visible beam diffraction limit. Bridging super-resolution fluorescence with vibrational spectroscopy, Chem-SIM opens a practical route to map organelle chemistry and microorganism metabolism—an enabling capability for cell biology, microbiology, and drug discovery.

A central challenge in wide-field photothermal imaging is the Skellam barrier where the difference of two Poisson measurements has variance that scales with the total detected fluorescence intensity.

Such shallow modulations are easily drowned by shot noise and dynamic-range compression. P-MLD addresses this challenge by fitting the full Hot/Cold photon statistics under the SIM forward model, recovering modulation amplitudes without introducing negative artifacts and with markedly lower noise floors. In a single *S. aureus*, the approach improves the FRC resolution from ~708 nm (F-MIP) to ~214 nm while preserving spectral features that match FTIR references. Conceptually, P-MLD is modality-agnostic and could be adapted to other pump–probe imaging schemes that suffer from similar brightness–modulation coupling.

In aqueous media, water absorption of mid-IR light overwhelms weak biomolecular signals and limits the modulation depth. Our PR gating exploits the temporal asymmetry between fast absorber heating/cooling and the slower, axially conducted water response. The two probe delays are chosen to sample the lipid-dominated peak and the water-dominated tail, and the difference cancels the water background while retaining target-specific contrast. Because water’s thermal response is strongly axial, effective optical sectioning becomes critical; SIM provides near-confocal sectioning in a camera-based format, making PR-gated chem-SIM a powerful tool for chemical imaging in liquid environments.

Chem-SIM provides the full mid-IR fingerprint spectrum that tells the chemical content of fluorescence-labeled bacteria or organelles. Such information lies beyond the reach of super-resolution fluorescence microscopy but is essential for organelle functional analysis. In Chem-SIM, the fluorescent reporter plays a dual role as a structural marker and a nanoscale thermometer. Pulsed mid-IR absorption encodes chemical bond information to the fluorescence contrast. Such capability turns fluorescence-resolved morphology into chemically interpretable maps, which is essential for organelle functional analysis and metabolic phenotyping.

We have shown that Chem-SIM images inherits the spatial resolution of the fluorescence channel. In F-MIP with a continuous wave probe, the point spread function (PSF) is set by the fluorescence PSF convolved with a thermal diffusion kernel accumulated over the detection window. In this work, our nanosecond-pulsed probe gates the signal predominantly during the prompt heating transient, and largely rejects the later, diffusion-driven relaxation. In PR-gated chem-SIM, the same transient selection strategy suppresses the more delocalized aqueous contribution in liquid, producing chemical maps at the SIM resolution in liquid environments.

We would point out several limitations of our technology. First, Chem-SIM relies on fluorescent reporters; the photon budget, photobleaching, and dye distribution can influence SNR and the interpretability of chemical maps. Our analysis and experiments indicate that P-MLD mitigates coupling between brightness and modulation, but absolute quantitation still requires careful control of labeling density and excitation conditions. Second, PR gating relies on differences in thermal transients that can be size- and shape-dependent; heterogeneity in droplet dimensions, morphology, or local thermal boundary conditions may bias the relative weighting of delays and should be characterized when comparing populations. Finally, spectral fidelity depends on accurate power normalization and suppression of atmospheric water lines; our weighted least-squares normalization is robust across reasonable parameter ranges, but seasonal humidity fluctuations necessitate periodic calibration of the power spectrum (or purging of the beam path) to stabilize baseline and line depths.

Several extensions are natural. Like 3D SIM^{45, 46}, 3D Chem-SIM could be realized by combining optical sectioning with depth-dependent delay selection in PR gating. In addition, by adaptive acquisition, i.e., tuning the IR wavenumber while performing time-lapse imaging, Chem-SIM could track organelle chemistry dynamically while minimizing dose and acquisition time.

Methods

Instrumentation

Chem-SIM was implemented on a lab-built upright wide-field microscope. A tunable mid-infrared QCL (Daylight Solutions, MIRcat) served as the pump, and a 520 nm nanosecond pulsed laser diode (Thorlabs, NPL52C) provided fluorescence excitation. Constrained by the probe repetition rate, the pump–probe sequence operated at 50 kHz. To maximize photothermal heating, the pump pulse width was set to 500 ns, and the pump–probe delay was tuned to the peak of the fluorescence-modulation response (**Supplementary Figure 11**).

Pump path. The mid-IR beam was focused onto CaF₂ substrates with a parabolic mirror (Thorlabs, MPD019-M03), producing an on-sample spot of approximately 50 μm diameter.

Probe/illumination path. The 520 nm probe was coupled through a fiber despeckler (Newport, F-DS-AFS105-FC/PC) via a focusing lens (L7, Thorlabs C260TMD-A) to reduce spatial coherence. After 200 \times beam expansion (L5–L6), the beam impinged on a digital micromirror device (DMD; Texas Instruments, DLP9500) at the blaze angle, carrying binary structured-illumination patterns. The patterned beam was Fourier-filtered with a lens (L4, $f = 500$ mm) and a pinhole mask (hexagonal aperture array) to pass the ± 1 diffraction orders. A relay (L2 $f = 180$ mm, L3 $f = 250$ mm) imaged the pattern to the sample through either a Nikon TUPlanFluor, NA 0.8 Air or Olympus LUMFLN, NA 1.1 Water objective. Epi-fluorescence was separated by a filter set (Ex 520/40, DM 550 LP, Em 550 LP), relayed by a tube lens (Thorlabs, TTL200), and recorded on an sCMOS camera (Andor Zyla 5.5) to form wide-field images.

Synchronization and timing. A digital delay pulse generator (Quantum Composers, Emerald 9254) provided the 50 kHz master clock and programmable trigger signals. A custom control program computed and issued the appropriate gated signals to the QCL, probe laser, and sCMOS exposure based on the selected camera integration time. The DMD was triggered by the camera’s global-exposure output to achieve an effective global shutter when running camera at its high-sensitivity rolling mode; its latency relative to the master clock was measured and actively compensated, ensuring the same number of pump–probe cycles per Hot/Cold frame. Both the pump–probe delay and the PR window were implemented by adjusting the QCL trigger delay relative to the probe in practice, thereby maintaining identical fluorescence-detection conditions across all acquisitions.

Spectroscopic Calibration and Normalization

Least squares spectral normalization. To compensate mid-IR power variation (including water-vapor lines) and remove baseline offsets while preserving sharp spectral features in 1D MIP/Chem-SIM spectra, we estimate a nonnegative normalized spectrum $u \geq 0$ and a scalar baseline b by solving a weighted least-squares problem with TV regularization

$$\min_{u \geq 0, b} \left\{ \sum_i (w_i u_i - y_i - b)^2 + \lambda \text{TV}(u) + \mu |b| \right\},$$

on the wavenumber grid ν_i . Where y_i is the measured raw spectrum and $w_i = p_i / \max_j p_j$ are weights from the on-sample IR power spectrum p_i . Here $\text{TV}(u)$ denotes the 1D total-variation semi-norm (absolute finite differences). This formulation is equivalent to a stabilized division by the power profile ($u \approx y/w$), while denoising edges and removing a constant offset. Solver detailed in **Supplementary Note 3**.

Across-dataset spectral comparison. For comparing multiple Chem-SIM/F-MIP spectra, area normalization (divide by the mean value over the full spectrum) is additionally applied to equalize overall intensity and emphasize relative band difference.

FTIR spectral normalization. Attenuated total reflection FTIR (ATR-FTIR, Thermo Scientific) spectra were exported as absorbance and converted to absorptance, then energy-weighted by multiplying by wavenumber to match the Chem-SIM/F-MIP energy-absorption convention, resampled onto the Chem-SIM/F-MIP wavenumber grid, and peak-normalized before overlay and comparison. Note: This procedure harmonizes dimensionality for shape comparison; absolute scaling in ATR depends on penetration depth and contact conditions and is not interpreted.

Poisson maximum-likelihood demodulation (P-MLD)

As mentioned in the main text, the Cold-state image corresponds to the baseline fluorescence map $x_{\text{Cold}} = x$, and the Hot fluorescence map is given by $x_{\text{Hot}} = m \odot x$. For the k -th illumination pattern s_k and point-spread-function (PSF) operator h , we model the imaging system by the linear operator

$$A_k(x) = h * (s_k \odot x) + b,$$

where $b \geq 0$ represents a slowly varying out-of-focus/background component added after convolution and $*$ denotes convolution. The expected photon counts (Poisson means) for the Cold/Hot frames are

$$\mu_k^{\text{Cold}} = A_k(x), \quad \mu_k^{\text{Hot}} = A_k(m \odot x).$$

The photothermal modulation image used as the chemical-contrast channel is defined as $z \equiv x - m \odot x$.

For each pattern $k = 1, \dots, 9$ (3 orientations \times 3 phases) and pixel j , the observed counts are $I_{k,j}^{\text{Cold}}, I_{k,j}^{\text{Hot}}$. Under shot-noise-limited detection, each pixel/frame is modeled as an independent Poisson random variable with mean $\mu_{k,j}^{\text{Cold}}$ or $\mu_{k,j}^{\text{Hot}}$, with probability mass function

$$p(I|\mu) = \frac{e^{-\mu} \mu^I}{\Gamma(I+1)}.$$

P-MLD jointly estimates z (equivalently x and m) by maximizing the joint Poisson log-likelihood⁴⁷:

$$\mathcal{L}(x, m) = \log \left[\prod_k^9 \prod_j^{w \times h} p(I_k^{\text{Cold}} | \mu_k^{\text{Cold}}) p(I_k^{\text{Hot}} | \mu_k^{\text{Hot}}) \right]$$

Where j indexes pixels, $w \times h$ is the image size, and $p(I|\mu)$ denotes the Poisson probability mass function. Algorithmic details are provided in **Supplementary Note 4**.

Sample preparation

Substrates. Double-side-polished calcium fluoride (CaF₂) disks (Crystran; 1 mm thick) were used as IR-transparent substrates for all samples. Disks were bonded with PMMA (polymethyl methacrylate) adhesive to the bottom aperture of a confocal imaging dish to form the observation window, then rinsed in 70% ethanol, washed with deionized water, and air-dried in a dust-free container.

HeLa and OVCAR5 cell culture and Lipi-Red labeling. HeLa and OVCAR5 cells were purchased from ATCC and cultured under standard conditions (37 °C, 5% CO₂) in their recommended media (e.g., DMEM for HeLa, RPMI-1640 for OVCAR-5) supplemented with 10% FBS (v/v) and 1% penicillin-streptomycin (v/v). For imaging, cells were seeded onto sterilized CaF₂ disks and cultured overnight for attachment. For fatty-acid treatment experiments, OVCAR5 cells were incubated with BSA-complexed PA-d₃₁ in de-lipid culture medium to promote lipid uptake and incorporation. PA-d₃₁ was first dissolved to 50 mM stock solution in DMSO and then diluted in de-lipid RPMI-1640 medium to 50 μM as the final concentration. The blank control group was cultured in the same medium condition without PA supply. After treatment, cells were washed 3× with pre-warmed PBS before staining. Lipid droplets were stained with Lipi-Red (Dojindo, 9 μmol L⁻¹, de-lipid medium) for 30 min at 37 °C, protected from light. After staining, cells were washed 3× with pre-warmed PBS. For live-cell Chem-SIM imaging of OVCAR5 cells, after staining and washing, the CaF₂ disk was transferred to a CO₂-independent live-cell imaging buffer (phenol red-free, HEPES-buffered medium) and allowed to equilibrate on the microscope stage for 30 min at ~20 °C room temperature before imaging (typically ~15 min per sample). For fixed-cell imaging, cells were then fixed in 4% paraformaldehyde for 30 min at room temperature, washed 3× with PBS, before imaging. For hyperspectral Chem-SIM of lipid chemistry under fatty-acid treatment, OVCAR5 cells were fixed after PA-d31 (or PA-free) incubation and subsequent

washing and then imaged following the same staining and handling steps unless otherwise specified.

R6G-labeled *E. coli* and *S. aureus*. Frozen stocks of *Escherichia coli* (*E. coli*) BW25113 and *Staphylococcus aureus* (*S. aureus*) ATCC6538 stored at –80 °C were streaked onto LB agar plates and incubated overnight at 37 °C. A single colony was then picked and inoculated into 3 mL of LB broth, followed by incubation at 37 °C for 3 hours to reach the logarithmic growth phase and 12 hours to reach the stationary phase. Bacterial cells were pelleted (5,000 x g, 5 min) and washed 3 times with PBS. The bacterial pellets were labeled with Rhodamine-6G (R6G) by incubating in 10 µM dye (in PBS) for 30 min at room temperature, protected from light, followed by 3 sterile water washes to reduce salt residues. A 3–10 µL aliquot was deposited onto a clean CaF₂ disk, gently spread to form a thin film, and air-dried for 10–15 min at room temperature, in the dark. Dried specimens were stored desiccated and imaged within several days.

Imaging data analysis and statistics

Imaging data were acquired and reconstructed with custom MATLAB (Mathworks) scripts. Hyperspectral Chem-SIM data were further processed and analyzed in ImageJ (Fiji). Lipid-droplet dynamic tracking was performed automatically using the TrackMate plugin (ImageJ/Fiji). Graphing, statistical summaries, and figure preparation were completed in MATLAB, OriginPro (OriginLab) and Adobe Illustrator.

Unless otherwise stated, quantitative results are reported as mean ± s.e.m. from *n* individual cocci or lipid droplets, as indicated in the corresponding figure legends. For statistical testing, SNR comparisons were performed using the Wilcoxon signed-rank test, log-stationary phase analyses were performed using a two-sample t-test, and MSD-based lipid-droplet motion analyses were performed using the Mann–Whitney U test (ranksum in MATLAB). statistical significance was annotated as: *, *p* < 0.05; **, *p* < 0.01; ***, *p* < 0.001; ****, *p* < 0.0001.

Data availability

All datasets generated and analyzed during this study are available from the corresponding author upon reasonable request.

Code availability

The weighted least-squares spectral normalization tool and P-MLD demodulation code are available as open-source software at <https://github.com/XXXXXX>. The implementation is also available via a Code Ocean capsule at <https://doi.org/XXXXXX>.

References

1. Valm, A.M. et al. Applying systems-level spectral imaging and analysis to reveal the organelle interactome. *Nature* **546**, 162–167 (2017).
2. Bar-Peled, L. & Kory, N. Principles and functions of metabolic compartmentalization. *Nature Metabolism* **4**, 1232–1244 (2022).

3. Huang, B., Bates, M. & Zhuang, X. Super-Resolution Fluorescence Microscopy. *Annual Review of Biochemistry* **78**, 993-1016 (2009).
4. Gustafsson, M.G.L. Surpassing the lateral resolution limit by a factor of two using structured illumination microscopy. *Journal of Microscopy* **198**, 82-87 (2000).
5. Wu, Y. & Shroff, H. Faster, sharper, and deeper: structured illumination microscopy for biological imaging. *Nature Methods* **15**, 1011-1019 (2018).
6. Chen, X. et al. Superresolution structured illumination microscopy reconstruction algorithms: a review. *Light: Science & Applications* **12**, 172 (2023).
7. Schermelleh, L. et al. Super-resolution microscopy demystified. *Nature Cell Biology* **21**, 72-84 (2019).
8. Dong, D. et al. Super-resolution fluorescence-assisted diffraction computational tomography reveals the three-dimensional landscape of the cellular organelle interactome. *Light: Science & Applications* **9**, 11 (2020).
9. Görlitz, F. et al. Mapping Molecular Function to Biological Nanostructure: Combining Structured Illumination Microscopy with Fluorescence Lifetime Imaging (SIM + FLIM). *Photonics* **4**, 40 (2017).
10. Winkelmann, H., Richter, C.P., Eising, J., Piehler, J. & Kurre, R. Correlative single-molecule and structured illumination microscopy of fast dynamics at the plasma membrane. *Nature Communications* **15**, 5813 (2024).
11. Zhanghao, K. et al. Super-resolution imaging of fluorescent dipoles via polarized structured illumination microscopy. *Nature Communications* **10**, 4694 (2019).
12. Zhanghao, K. et al. High-dimensional super-resolution imaging reveals heterogeneity and dynamics of subcellular lipid membranes. *Nature Communications* **11**, 5890 (2020).
13. Cheng, J.-X. et al. Advanced vibrational microscopes for life science. *Nature Methods* **22**, 912-927 (2025).
14. Freudiger, C.W. et al. Label-Free Biomedical Imaging with High Sensitivity by Stimulated Raman Scattering Microscopy. *Science* **322**, 1857-1861 (2008).
15. Zhang, D. et al. Depth-resolved mid-infrared photothermal imaging of living cells and organisms with submicrometer spatial resolution. *Science Advances* **2**, e1600521 (2016).
16. Qian, N. et al. Illuminating life processes by vibrational probes. *Nature Methods* **22**, 928-944 (2025).
17. Lv, X., Gong, L., Lin, S., Jin, P. & Huang, Z. Super-resolution stimulated Raman scattering microscopy with the phase-shifted spatial frequency modulation. *Opt. Lett.* **47**, 4552-4555 (2022).
18. Guilbert, J. et al. Label-free super-resolution stimulated Raman scattering imaging of biomedical specimens. *Advanced Imaging* **1**, 011004 (2024).
19. Zhao, S. et al. Computational field-resolved coherent chemical imaging. *Nature Communications* **16**, 7406 (2025).
20. Bai, Y. et al. Ultrafast chemical imaging by widefield photothermal sensing of infrared absorption. *Science Advances* **5**, eaav7127 (2019).
21. Zhang, D. et al. Bond-selective transient phase imaging via sensing of the infrared photothermal effect. *Light: Science & Applications* **8**, 116 (2019).
22. Xia, Q. et al. Single virus fingerprinting by widefield interferometric defocus-enhanced mid-infrared photothermal microscopy. *Nature Communications* **14**, 6655 (2023).
23. Tamamitsu, M. et al. Mid-infrared wide-field nanoscopy. *Nature Photonics* **18**, 738-743 (2024).

24. Xia, Q., Yin, J., Guo, Z. & Cheng, J.-X. Mid-Infrared Photothermal Microscopy: Principle, Instrumentation, and Applications. *The Journal of Physical Chemistry B* **126**, 8597-8613 (2022).

25. Zhao, J. et al. Bond-selective intensity diffraction tomography. *Nature Communications* **13**, 7767 (2022).

26. Tamamitsu, M. et al. Label-free biochemical quantitative phase imaging with mid-infrared photothermal effect. *Optica* **7**, 359-366 (2020).

27. Zong, H. et al. Background-Suppressed High-Throughput Mid-Infrared Photothermal Microscopy via Pupil Engineering. *ACS Photonics* **8**, 3323-3336 (2021).

28. Zhang, Y. et al. Fluorescence-Detected Mid-Infrared Photothermal Microscopy. *Journal of the American Chemical Society* **143**, 11490-11499 (2021).

29. Li, M. et al. Fluorescence-Detected Mid-Infrared Photothermal Microscopy. *Journal of the American Chemical Society* **143**, 10809-10815 (2021).

30. Prater, C.B. et al. Widefield Super-Resolution Infrared Spectroscopy and Imaging of Autofluorescent Biological Materials and Photosynthetic Microorganisms Using Fluorescence Detected Photothermal Infrared (FL-PTIR). *Applied Spectroscopy* **78**, 1208-1219 (2024).

31. Jia, D. et al. 3D Chemical Imaging by Fluorescence-detected Mid-Infrared Photothermal Fourier Light Field Microscopy. *Chemical & Biomedical Imaging* **1**, 260-267 (2023).

32. Ao, J. et al. In vivo mapping organellar metabolism by optical-boxcar enhanced fluorescence-detected mid-infrared photothermal microscopy. *arXiv preprint arXiv:2504.04305* (2025).

33. Fu, P. et al. Breaking the diffraction limit in molecular imaging by structured illumination mid-infrared photothermal microscopy. *Advanced Photonics* **7**, 036003 (2025).

34. Toda, K. & Ideguchi, T. Ludwig–Soret microscopy with the vibrational photothermal effect. *Proceedings of the National Academy of Sciences* **122**, e2510703122 (2025).

35. Huang, F. et al. Video-rate nanoscopy using sCMOS camera–specific single-molecule localization algorithms. *Nature Methods* **10**, 653-658 (2013).

36. Skellam, J.G. The Frequency Distribution of the Difference between Two Poisson Variates Belonging to Different Populations. *Journal of the Royal Statistical Society* **109**, 296-296 (1946).

37. Barrett, H.H. et al. Maximum-Likelihood Methods for Processing Signals From Gamma-Ray Detectors. *IEEE Transactions on Nuclear Science* **56**, 725-735 (2009).

38. Nieuwenhuizen, R.P.J. et al. Measuring image resolution in optical nanoscopy. *Nature Methods* **10**, 557-562 (2013).

39. Shuster, S.O., Curtis, A.E. & Davis, C.M. Optical Photothermal Infrared Imaging Using Metabolic Probes in Biological Systems. *Analytical Chemistry* **97**, 8202-8212 (2025).

40. Tan, Y. et al. Metabolic reprogramming from glycolysis to fatty acid uptake and beta-oxidation in platinum-resistant cancer cells. *Nature Communications* **13**, 4554 (2022).

41. Nieman, K.M. et al. Adipocytes promote ovarian cancer metastasis and provide energy for rapid tumor growth. *Nature Medicine* **17**, 1498-1503 (2011).

42. Park, C., Lim, J.M., Hong, S.-C. & Cho, M. Monitoring the synthesis of neutral lipids in lipid droplets of living human cancer cells using two-color infrared photothermal microscopy. *Chemical Science* **15**, 1237-1247 (2024).

43. Shubeita, G.T. et al. Consequences of Motor Copy Number on the Intracellular Transport of Kinesin-1-Driven Lipid Droplets. *Cell* **135**, 1098-1107 (2008).

44. Dou, W., Zhang, D., Jung, Y., Cheng, J.X. & Umulis, D.M. Label-free imaging of lipid-droplet intracellular motion in early *Drosophila* embryos using femtosecond-stimulated Raman loss microscopy. *Biophys J* **102**, 1666-1675 (2012).
45. Cao, R. et al. Open-3DSIM: an open-source three-dimensional structured illumination microscopy reconstruction platform. *Nature Methods* **20**, 1183-1186 (2023).
46. Chen, Q. et al. Fast, three-dimensional, live-cell super-resolution imaging with multiplane structured illumination microscopy. *Nature Photonics* **19**, 567-576 (2025).
47. Chakrova, N., Rieger, B. & Stallinga, S. Deconvolution methods for structured illumination microscopy. *J. Opt. Soc. Am. A* **33**, B12-B20 (2016).

Acknowledgements

This work is supported by NIH grants R35GM136223, R01AI141439, R33CA287046, and by grant number 2023-321163 from the Chan Zuckerberg Initiative DAF, an advised fund of Silicon Valley Community Foundation.

Author information

Authors and Affiliations

Department of Electrical and Computer Engineering, Boston University, Boston, USA

Dashan Dong, Danchen Jia, Jianpeng Ao, George Abu-Aqil, Meng Zhang, Qing Xia and Ji-Xin Cheng

Photonics Center, Boston University, Boston, USA

Dashan Dong, Danchen Jia, Jianpeng Ao, Meng Zhang, Qing Xia and Ji-Xin Cheng

Department of Chemistry, Boston University, Boston, USA

Xinyan Teng, Biwen Gao, and Ji-Xin Cheng

Department of Biomedical Engineering, Boston University, Boston, USA

Ji-Xin Cheng

Contributions

D.D. and J.X.C. conceived the project. J.X.C. supervised the research and revised the manuscript. D.D. designed and built the instrumentation, wrote the control software, developed the reconstruction algorithms, and performed all experiments. D.C.J. assisted in the data acquisition and hyperspectral chemical imaging. D.C.J., X.Y.T., J.P.A., and Q.X. conducted substantive discussions on data analysis. X.Y.T., J.P.A., and B.W.G prepared and provided the cell samples, while G.A.-A. and M.Z. prepared and provided the bacterial samples. All authors discussed the results and approved the final manuscript.

Corresponding author

Ji-Xin Cheng, jxcheng@bu.edu

Ethics declarations**Competing interests**

JXC declare financial interest with Photothermal Spectroscopy Corp, which did not fund this work. Other authors declare no competing interests.

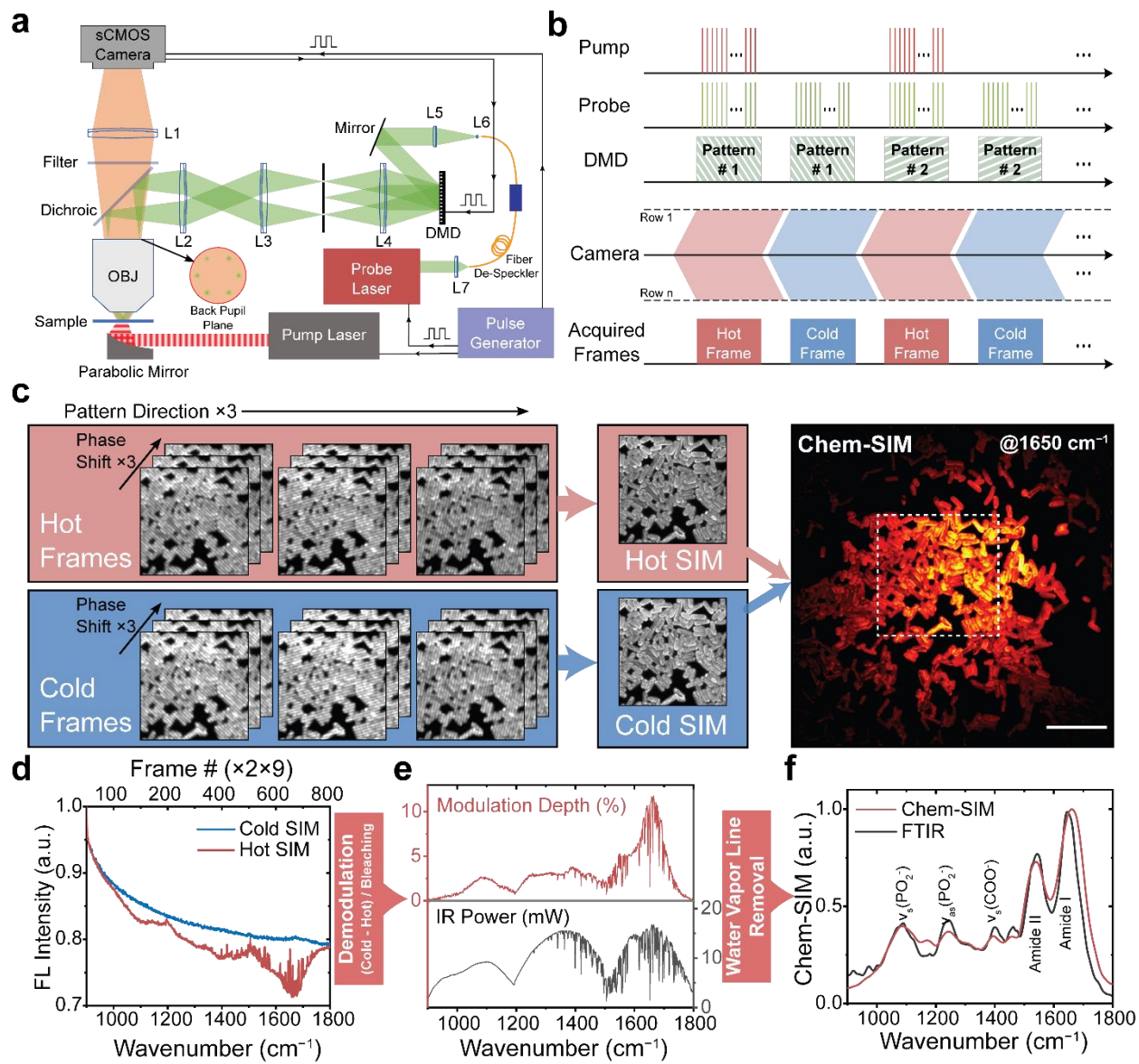


Figure 1 Principle and workflow of Chem-SIM. (a) Schematic of the Chem-SIM microscope. (b) Timing diagram for pump, probe, DMD patterns and synchronized camera acquisition. (c) Reconstruction workflow demonstrated using R6G-labelled *E. coli* at $\nu=1650\text{ cm}^{-1}$; scale bar, 10 μm . (d) Mean fluorescence intensity within the dashed boxed region for hot-SIM and cold-SIM hyperspectral stacks. (e) Bleaching-corrected fluorescence modulation-depth spectrum and on-sample IR power. (f) Chem-SIM absorption spectrum after water-vapor line removal by weighted least-squares normalization, compared with a normalized reference FTIR spectrum.

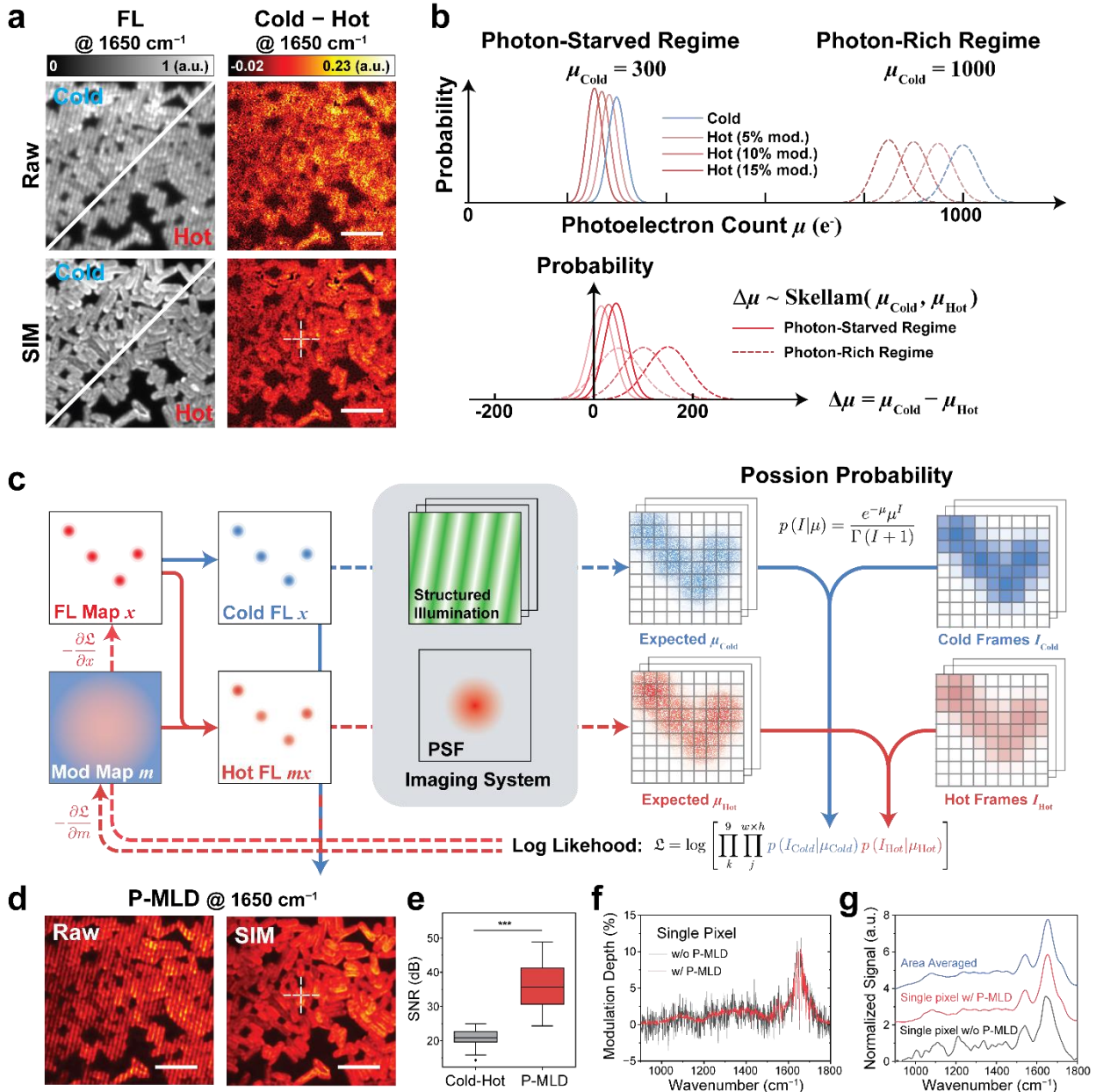


Figure 2 Poisson maximum-likelihood demodulation (P-MLD) enabled high-quality Chem-SIM. (a) Cold, Hot, and Cold - Hot images from the dashed boxed region in **Figure 1c**, showing that simple subtraction yields poor SNR in both raw patterned and SIM-reconstructed modulation images. (b) Schematic 1D intensity distributions illustrating loss of modulation contrast when subtracting Poisson-distributed hot and cold photon counts; the pixel-wise difference follows a Skellam distribution that mixes contributions from regions with different fluorescence levels and modulation depths. (c) Image-formation model and P-MLD workflow: a fluorescence map x and fractional modulation map m generate hot fluorescence mx ; structured illumination and the microscope PSF produce expected cold and hot photon counts μ_{Cold} and μ_{Hot} , and x and m are jointly estimated by maximizing the Poisson log-likelihood. (d) P-MLD improve the SNR in both raw patterned and SIM-reconstructed modulation images. (e) SNR comparison between Cold - Hot and P-MLD. (f) Single pixel modulation-depth spectrum at the position of dashed cross w/o and w/ P-MLD. (g) Area-averaged and single-pixel Chem-SIM spectra showing that P-MLD enables high-SNR vibrational fingerprints at the single-pixel level. Scale bars, 5 μm .

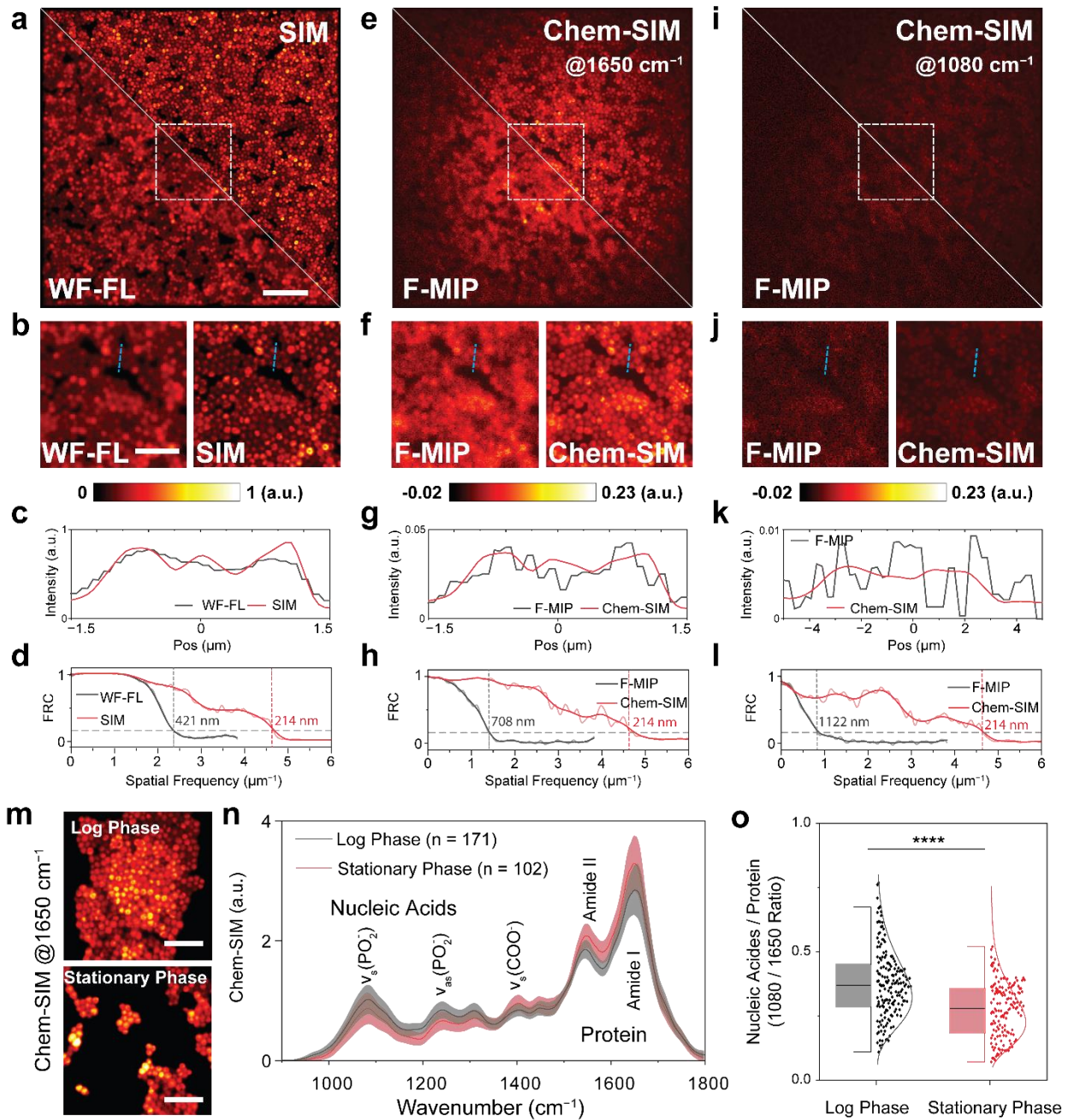


Figure 3 Spatial and spectroscopic Chem-SIM mapping of *S. aureus*. (a-d) Wide-field fluorescence (WF-FL) and SIM reconstruction of the same field of view, shown as (a) split-views overlays, (b) zoomed-in crops of the dashed box, (c) line profiles along the blue dashed lines, and (d) Fourier ring correlation (FRC) curves quantifying the resolution gain. (e-h) Corresponding F-MIP (Cold-Hot) and Chem-SIM (with P-MLD) images at the amide-I band ($\nu=1650\text{ cm}^{-1}$), displayed with the same (e) split-view, (f) zoom, (g) line-profile and (h) FRC layout. (i-l) F-MIP and Chem-SIM images at the nucleic-acid band ($\nu=1080\text{ cm}^{-1}$), likewise shown as (i) split views, (j) zooms, (k) line profiles, and (l) FRC analysis. (m-o) Growth-phase analysis: (m) Chem-SIM maps @ 1650 cm^{-1} for stationary-phase and log-phase populations; (n) population-averaged single-bacterium Chem-SIM spectra (mean \pm s.e.m.) for the two phases; (o) distribution of the $1080/1650\text{ cm}^{-1}$ Chem-SIM intensity ratio (nucleic acids/protein) comparing log-phase and stationary-phase cells. Scale bars, $10\text{ }\mu\text{m}$ (a) and $5\text{ }\mu\text{m}$ (b, m).

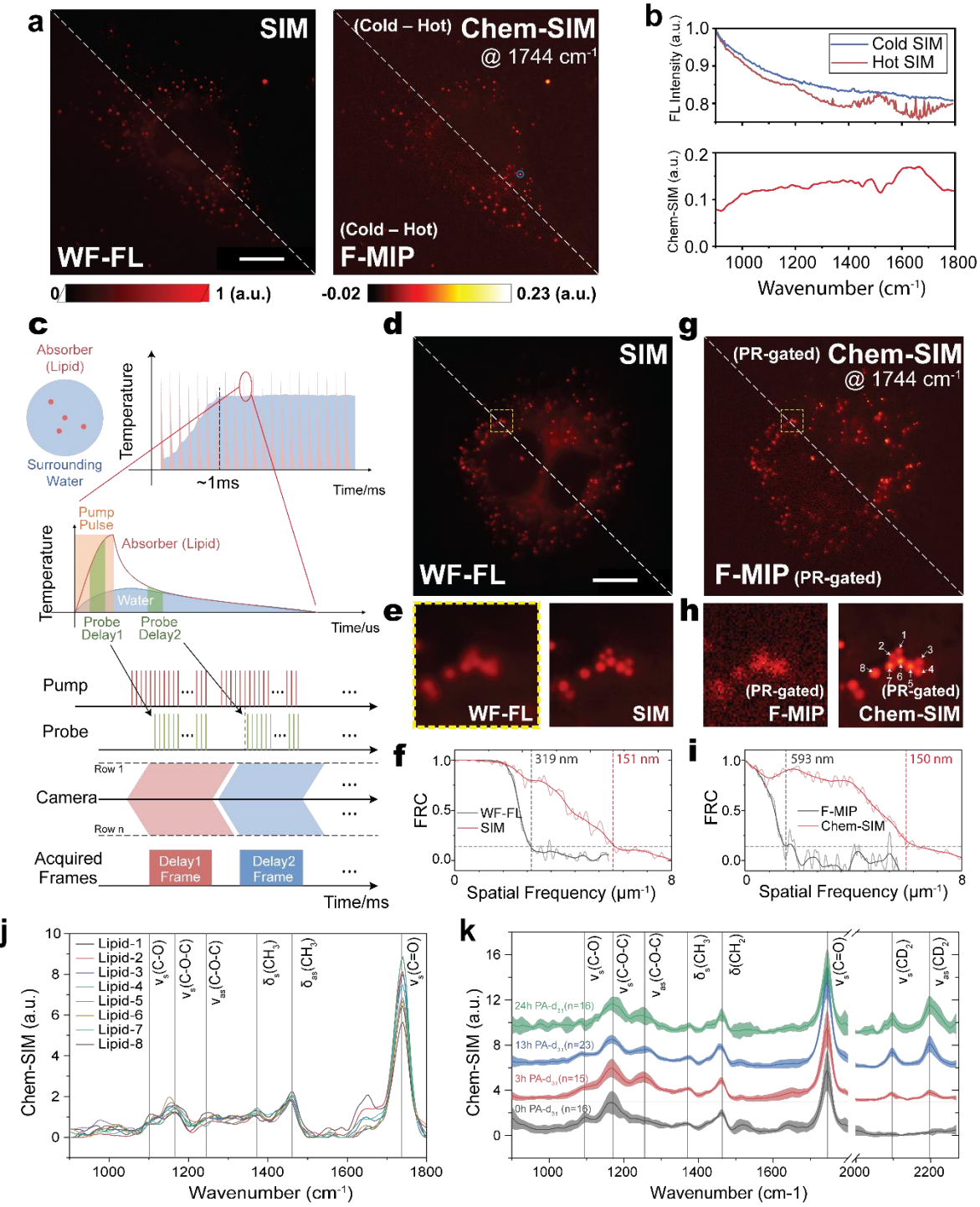


Figure 4 Background-suppressed Chem-SIM of cells in aqueous environments via photothermal relaxation (PR) gating. (a) Hela cell imaged by WF-FL and SIM (split view) and corresponding F-MIP and Chem-SIM at 1744 cm⁻¹ using the hot-cold mode. (b) Hyperspectral Chem-SIM from the blue-circled lipid droplet in (a), showing Cold-/Hot- SIM intensity traces and corresponding normalized spectrum. (c) Conceptual diagram and timing scheme of PR gating. (d-f) WF-FL/SIM reconstructions for comparison, using frames acquired at delay 2: (d) WF-FL/SIM split view, (e) zoomed-in of the yellow dashed box, and (f) FRC analysis. (g-i) PR-gated F-MIP and Chem-SIM images at 1744 cm⁻¹: (g) full-field view, (h) zoomed-in view, and (i) FRC analysis. (j) Single-droplet Chem-SIM spectra from the eight droplets in (h), showing consistent ester C=O peaks, strongly suppressed out-of-band background, and additional lipid bands with varying relative amplitudes. (k) Chem-SIM spectra of PA-d₃₁-treated OVCAR5 cells under different incubation conditions. Scale bars, 10 μm.

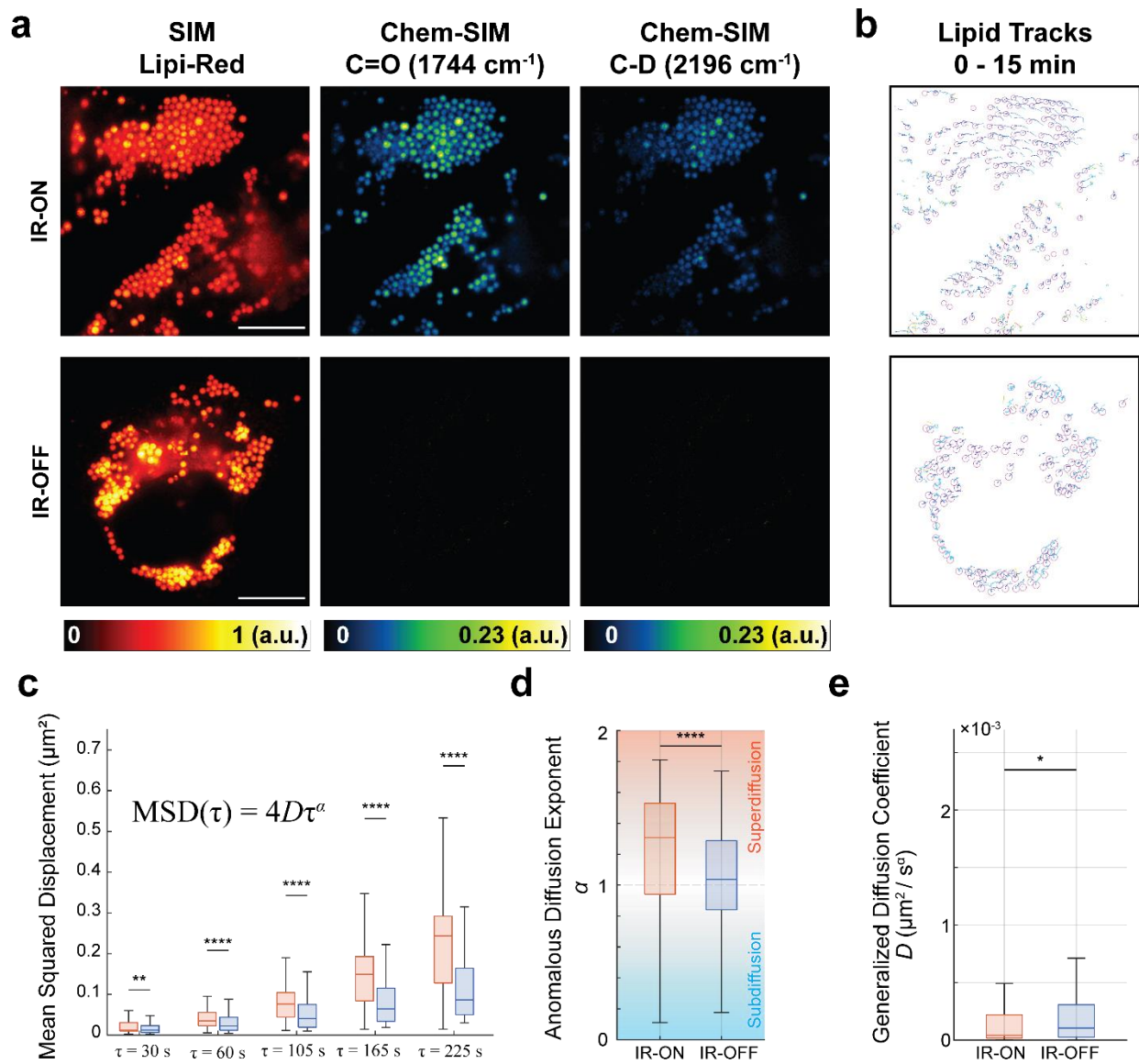


Figure 5 Chem-SIM imaging on PA-d₃₁-treated live OVCAR5 cells. (a) SIM Lipi-Red images (left), Chem-SIM map at the ester C=O band (1744 cm^{-1} , middle) and the C-D band (2196 cm^{-1} , right). (b) Lipid-droplet tracks over 0–15 min for PA-d₃₁-loaded OVCAR5 cells imaged with the IR pump on (IR-ON, top) or off (IR-OFF, bottom). (c) Mean squared displacement (MSD) of individual droplets versus lag time τ , summarized as box plots for IR-ON (orange) and IR-OFF (blue). (d) Distribution of the anomalous diffusion exponent α for IR-ON and IR-OFF trajectories, with background shading indicating subdiffusion ($\alpha < 1$) and superdiffusion ($\alpha > 1$) regimes. (e) Generalized diffusion coefficient D for the same trajectories, showing modest changes between IR-ON and IR-OFF conditions. Error bars and boxes denote the spread across all tracked droplets. Scale bars, 10 μm .